A Uniform Multi-mode Fused Framework for Velocity Field Estimation in Ultrasound Imaging

Hailong Li, Liansheng Wang, and Yinran Chen(✉)

Department of Computer Science and Technology, School of Informatics, Xiamen University, Xiamen 361102, China.
✉ Corresponding author: yinran_chen@xmu.edu.cn

Abstract. Velocity field estimation, or motion tracking, is the key to characterizing tissue function in ultrasound imaging. Current velocity field estimation remains challenging in cross-range motion tracking due to the less sensitivity of ultrasound in this dimension. In addition, there is a lack of a uniform framework for different imaging schemes, such as linear array with rectangular scanning, phased array with sector scanning, and matrix array with volumetric scanning. This paper proposes a uniform multi-mode fused framework for tissue velocity field estimation. This framework integrates multiple modes of pair-wise optical flows, Doppler, and speckle consistency in ultrasound to improve the accuracy of cross-range velocity estimation. Furthermore, the uniform framework is adapted to different arrays and imaging schemes for various application scenarios. Extensive *in-silico* experiments on homemade and public datasets demonstrate the effectiveness of the proposed framework and the outperformance of our method when compared with a window-based method and an energy function optimization-based method. Particularly, our method improves the accuracy of cross-range velocity estimation by 8.84%, 19.21%, and 10.94% in three cross-sectional views of the public cardiac dataset when compared with the energy function optimization-based method.

Keywords: Ultrasound · Motion estimation · Optical flow · Doppler.

1 Introduction

Ultrasound imaging has emerged as a fundamental and powerful clinical diagnostic tool that provides anatomical and functional images of tissues and organs. Anatomical images are commonly presented in B-mode, whereas the functional information is provided in multiple ways. For example, elastography can characterize tissue pathologies by estimating their mechanical properties to classify dysfunctional regions [19]. A key step of functional characterization in ultrasound is velocity field estimation, or motion tracking, as different tissues or abnormal components exhibit distinct viscoelastic properties [2]. Velocity field estimation is typically achieved by processing pre and post-motion frames by leveraging the unique data characteristics of ultrasound images. Current methods are broadly

categorized into window-based, energy function optimization-based, and deep learning-based approaches.

Window-based methods, such as normalized cross-correlation (NCC) and zero-phase techniques, focus on local displacements by matching post-motion patches to a referenced frame [14, 12]. These methods are particularly effective for in-range motion tracking. However, they struggle with cross-range motion estimation due to the poorer spatial resolution in this dimension, where the point spread function (PSF) is wider compared to that in the in-range dimension. Additionally, window-based methods face challenges in estimating large motions due to speckle decorrelation [2]. On the other hand, energy function optimization-based methods formulate velocity field estimation as a global optimization problem including physical constraints and regularization such as Doppler and ultrasonic optical flow [20, 15, 16, 4, 13]. These methods are more robust to speckle decorrelation and noise but tend to smooth and underestimate velocity fields due to regularization. Deep learning-based methods have recently emerged as a promising alternative, offering the ability to adapt to the complexity of ultrasound imaging scenarios through deep neural networks [7, 10, 18, 9, 21]. However, supervised deep learning approaches heavily rely on the quality of training data and labels, which are often unavailable in *in-vivo* datasets [8, 23]. To address this, semi-supervised or unsupervised methods have been proposed to facilitate advancements in ultrasound motion tracking [6, 5, 22].

Current ultrasound velocity field estimation remains challenging raised by the following issues: (1) Inaccurate estimation of cross-range velocity components due to a lower motion sensitivity in this dimension. (2) Out-of-plane motion in the two-dimensional (2D) imaging. (3) The lack of a uniform framework for velocity field estimation across different imaging schemes, such as linear, phased, convex, and matrix arrays. This paper proposes a uniform multi-mode fusion framework applicable to various ultrasound imaging schemes, with enhanced cross-range velocity accuracy. These multi-mode constraints, combined with rational regularization, are integrated into a flexible framework that can be adapted to various schemes, preserving ultrasound data characteristics and eliminating the need for scan conversion, especially in time-consuming volumetric imaging. The main technical contributions are as follows: (1) The introduction of multi-mode fused constraints, including tissue Doppler, pair-wise optical flows, and speckle consistency, to estimate tissue velocity fields. (2) The development of a uniform framework that integrates these constraints and adapts to different imaging schemes. (3) The demonstration of the framework's effectiveness through extensive *in-silico* validations, showcasing its ability to estimate velocity fields without losing intrinsic ultrasound characteristics.

2 Methods

2.1 Modified Doppler Estimation

The sequential ultrasound beam emissions with an order of $[1, ..., N, 1, ..., N]$ (N is the number of angles) cause the PSF to rotate in one direction and bias

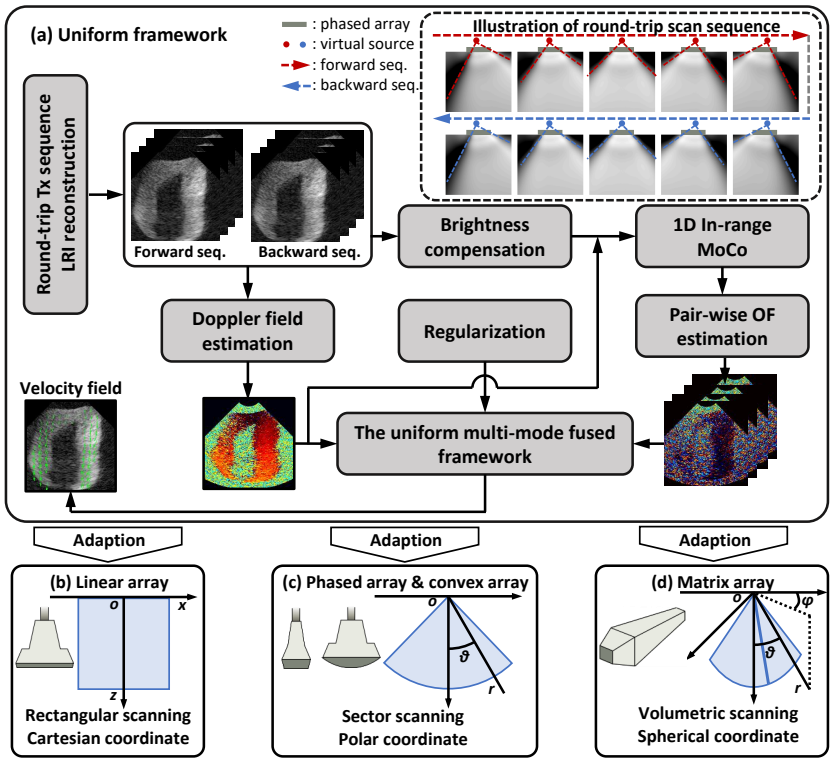

Fig. 1. (a) is the uniform framework for velocity field estimation. The framework is adapted to (b) linear array imaging with rectangular scanning, (c) phased and convex array with sector scanning, and (d) matrix array with volumetric scanning.

Doppler estimation [17]. To address this, a round-trip emission with an order of $[1, ..., N, N, ..., 1, 1, ...]$ [3, 4] is adopted. Therefore, the Doppler velocity v_{dp} is given by [17]:

$$v_{dp} = -\frac{f_{prf} \cdot c}{4\pi \cdot f_0} \cdot \frac{1}{2} \angle(r_{fd} \cdot r_{bd}), \tag{1}$$

where $f_{prf} = 5$ kHz is the pulse repetition frequency, f_0 is the center frequency, and $c = 1540$ m/s is the speed of sound in tissue. $\angle(r_{fd} \cdot r_{bd})$ computes the angle of the complex-valued coefficient where the product cancels out the pseudo-velocity caused by PSF rotation. The factor of $1/2$ is necessary to scale the phase from $r_{fd} \cdot r_{bd}$. The minus sign ensures consistency with the imaging coordinate.

2.2 Uniform Framework

Fig. 1(a) presents the diagram of the uniform framework that contains the constraints of Doppler, pair-wise optical flow, brightness compensation (BnCo), 1D in-range motion compensation (MoCo), and regularization.

Doppler Constraint. The Doppler field v_{dp} obtained in Eq. 1 is the projection of the unknown velocity field $\mathbf{v}$ onto the in-range dimension $\mathbf{n}_{dp}$, where $\mathbf{n}_{dp}$ is the unit vector of Doppler direction. Therefore, the Doppler constraint minimizes the following error term [16, 4]:

$$E_{dp} = w_0 \int_{\Omega} \left(\langle \mathbf{n}_{dp} \, , \mathbf{v} \rangle - v_{dp} \right)^2 d\Omega, \tag{2}$$

where w_0 is the weight of the constraint. Ω is the region-of-interest (ROI).
Brightness Compensation (BnCo). Multi-angle plane or diverging wave transmissions result in non-uniform sound fields, showing stronger fields along the beam's main axis and weaker fields elsewhere. This variation violates the brightness constancy assumption of optical flow, especially for fast-moving targets. BnCo is proposed to compensate for non-uniform sound fields in the round-trip scan sequence. Since measuring the true sound fields is non-trivial, we simulate them using Field II [11] and equalize the images to quasi-constant brightness.
1D In-Range MoCo. The directions of optical flow velocities depend on the spatial gradients of images, which may collide with the in-range Doppler velocities. To mitigate such collision and make the pair-wise optical flow constraints more focused on cross-range estimation, 1D in-range MoCo is performed on the images after BnCo:

$$\mathbf{I}_{moco}(\mathbf{r}) = \mathbf{I}_{moco}(\mathbf{r} + \Delta\mathbf{r}) e^{-j4\pi \Delta\mathbf{r} f_0 / c} \tag{3}$$

where $\mathbf{r}$ denotes the in-range dimension and $\Delta\mathbf{r}$ is the displacement. Here the symbols of the cross-range dimension are omitted for a clearer interpretation.
Pair-Wise Optical Flow Constraints. The images after BnCo and 1D MoCo primarily exhibit cross-range motions. In a round-trip sequence, the two images from the same angle have similar beam characteristics. As a result, the N pairs of images generate N pair-wise optical flow fields at different time scales:

$$v_{of}^{(i)} = -\frac{(\mathbf{I}^{(2N+1-i)} - \mathbf{I}^{(i)}) \cdot f_{prf}}{(2N - 2i + 1) \parallel \nabla \mathbf{I}^{(i)} \parallel}, \quad i = 1, 2, ..., N \tag{4}$$

where $\parallel \nabla \mathbf{I}^{(i)} \parallel$ computes the normalized spatial gradients of images. The constraints minimizes the following error term:

$$E_{of}^{(i)} = w_i \int_{\Omega} \left(\langle \mathbf{n}_{of} \, , (\mathbf{v} - v_{dp}) \rangle - v_{of}^{(i)} \right)^2 d\Omega, \tag{5}$$

where w_i is the weight of the i-th pair constraint. $\mathbf{n}_{of} = \frac{\nabla \mathbf{I}^{(i)}}{\| \nabla \mathbf{I}^{(i)} \|}$ is the unit vector indicating the direction of v_{of} determined by the spatial gradients.
Regularization. In the framework, we use a second-order smoothness regularization to ensure the smoothness of the velocity field estimates. The regularization term E_{smh} is formulated according to the characteristics of the following imaging schemes and coordinates.

Finally, the uniform multi-mode fused framework is formulated as a global optimization baseline: $\mathbf{v} = \arg\min \left(E_{dp} + \sum_{i=1}^{N} E_{of}^{(i)} + E_{smh} \right)$.

2.3 Adaptation

Linear Array with Rectangular Scanning. Fig. 1(b) shows that linear array imaging reconstructs images in the Cartesian coordinate. The velocity field is denoted as $\mathbf{v} = [v_x, v_z]$, where x and z represent the cross-range and in-range dimensions, respectively. The Doppler constraint is the same to Eq. 2 with $\mathbf{n}_{dp} = [0, 1]$. The pair-wise optical flow constraint and smoothness are:

$$E_{of}^{(i)} = w_i \int_{\Omega} \left(\frac{\mathbf{I}_x^{(i)} v_x + \mathbf{I}_z^{(i)} (v_z - v_{dp})}{\parallel \nabla \mathbf{I}^{(i)} \parallel} - v_{of}^{(i)} \right)^2 d\Omega, \tag{6}$$

$$E_{smh} = \lambda \sum_{m \in \{x,z\}} \int_{\Omega} (\partial_x^2 v_m)^2 + 2(\partial_{xz}^2 v_m)^2 + (\partial_z^2 v_m)^2 d\Omega. \tag{7}$$

Note that Eqs. 2, 6, and 7 also work for other imaging schemes if their images are scan-converted to the 2D/3D Cartesian coordinates.

Phased Array with Sector Scanning. Fig. 1(c) shows phased array imaging in the polar coordinate. The velocity field is denoted as $\mathbf{v} = [v_r, v_\theta]$, where r and θ denote the in-range and cross-range dimensions, respectively. The constraints and regularization are amended to:

$$E_{dp} = w_0 \int_{\Omega} (r d_r v_r + d_\theta v_\theta - r v_{dp})^2 d\Omega, \tag{8}$$

$$E_{of}^{(i)} = w_i \int_{\Omega} \left(\frac{r \mathbf{I}_r^{(i)} (v_r - v_{dp}) + \mathbf{I}_\theta^{(i)} v_\theta}{\parallel \nabla \mathbf{I}^{(i)} \parallel} - r v_{of}^{(i)} \right)^2 d\Omega, \tag{9}$$

$$E_{smh} = \lambda \sum_{m \in \{r,\theta\}} \int_{\Omega} \Big((r^2 \partial_r^2 v_m)^2 + 2(r \partial_{r,\theta}^2 v_m)^2 + (\partial_\theta^2 v_m)^2 \Big) d\Omega. \tag{10}$$

Matrix Array with Volumetric Scanning. The velocity fields of matrix array imaging in a 3D spherical coordinate are denoted as $\mathbf{v} = [v_r, v_\theta, v_\phi]$, where r is the in-range dimension and $[\theta, \phi]$ represent the 2D cross-range dimensions (Fig. 1(d)). The corresponding terms are amended as follows:

$$E_{dp} = w_0 \int_{\Omega} (r d_r v_r + r d_\theta v_\theta + r d_\phi v_\phi - r v_{dp})^2 d\Omega, \tag{11}$$

$$E_{of}^{(i)} = w_i \int_{\Omega} \left(\frac{\sin\theta \mathbf{I}_\theta^{(i)} v_\theta + \mathbf{I}_\phi^{(i)} v_\phi + r \sin\theta \mathbf{I}_r^{(i)} (v_r - v_{dp})}{\parallel \nabla \mathbf{I}^{(i)} \parallel} - r \sin\theta v_{of}^{(i)} \right)^2 d\Omega, \tag{12}$$

$$\begin{aligned} E_{smh} = \lambda \sum_{m \in \{r,\theta,\phi\}} \int_{\Omega} \Big(& 2r \sin^2\theta \partial_r v_m + r^2 \sin^2\theta \partial_r^2 v_m + \sin\theta \cos\theta \partial_\theta v_m \\ & + \sin^2\theta \partial_\theta^2 v_m + \partial_\phi^2 v_m \Big) d\Omega. \end{aligned} \tag{13}$$

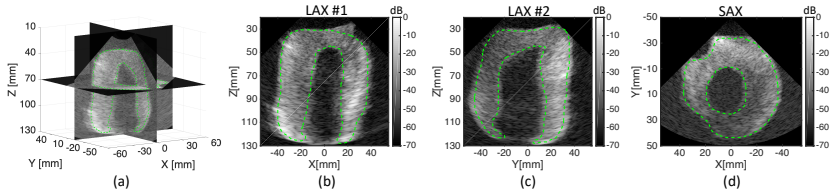

Fig. 2. Illustration of the cross-sections in STRAUS.

Table 1. Configurations and parameters of different imaging schemes

Probe	Type	f_0 [MHz]	No. elements	No. angles	Imaging grid (λ is the wavelength)
Linear	L11-4v	6.25	128	9	393 × 393 (pixel size: $(\lambda/2)^2$)
Phased	P4-2v	2.75	64	9	192 lines between $\pm(45^\circ)$, $dr = \lambda/2$
Matrix	-	3	32 × 32	3 × 3	192 × 192 lines between $\pm(30^\circ)$

3 Experiments and Results

3.1 Imaging Sequence, Dataset, and Comparison

Table 1 lists the configurations of the imaging schemes in Field II [11]. In addition, for linear array imaging, the probe pitch is 0.3 mm. The maximal steering angle of plane waves is $\pm 10^\circ$. For phased array imaging, the probe pitch is 0.3 mm. The maximal steering angle of diverging waves is $\pm 16^\circ$. For the matrix imaging, the probe pitch is 0.3 mm × 0.3 mm. The experiments were conducted on two numerical phantoms. The first is a spinning disk with four anechoic cylinders, mimicking a heart with four chambers [17, 4]. The radii of the disk and inclusion are 50 mm and 15 mm, respectively. The disk was rotating clockwise at maximal outer linear velocities of [10, 15, 20] cm/s for linear array imaging and [10, 15, 20, 25, 30] cm/s for phased array imaging. Scatterers were randomly distributed in the imaging field according to a density of 10 per resolution cell. The second dataset is the public 3D strain assessment in ultrasound (STRAUS) generated from *in-vivo* cardiac images obtained with high-precision electro/mechanical models [1]. Fig. 2 illustrates two long-axis (LAX) and one short-axis (SAX) cross-sections of STRAUS. For all the datasets, delay-and-sum (DAS) beamforming with dynamic receive focusing were applied to obtain the images.

We compared our method with NCC [14] and VVI [16] to evaluate its performance. NCC and VVI were chosen because they are representative of window-based and optimization-based methods, respectively. Moreover, both methods can be extended to linear and phased imaging, which aligns with the main goal of providing a unified framework for different imaging schemes. The normalized root mean square error (nRMSE) and the coefficient of determination R^2 (see Eq. 13 and Eq. 14 in [24]) are used to evaluate the estimated velocity fields.

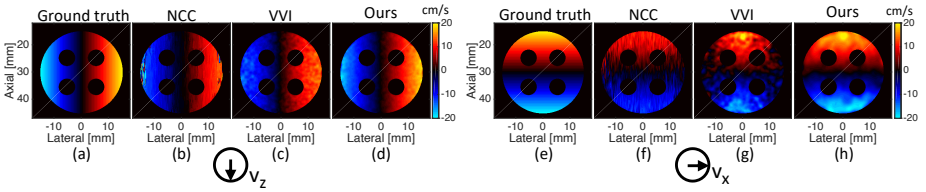

Fig. 3. Velocity fields of the spinning disk at a maximal linear velocity of 20 cm/s in the linear array imaging. (a)-(d) are the axial (in-range) velocity fields of ground truth, NCC, VVI, and our method. (e)-(h) are the lateral (cross-range) velocity fields.

Table 2. nRMSE and R^2 of the velocity fields in the phased array imaging.

Field of view	LAX #1			LAX #2			SAX		
Method	NCC	VVI	Ours	NCC	VVI	Ours	NCC	VVI	Ours
nRMSE(in,%) ↓	10.21	6.81	**4.79**	20.65	10.99	**8.10**	25.35	17.98	**12.92**
nRMSE(cross,%) ↓	24.46	18.59	**9.75**	33.46	31.81	**12.6**	36.37	25.20	**14.26**
R^2(in) ↑	0.77	0.94	**0.97**	0.68	0.83	**0.90**	0.21	0.59	**0.68**
R^2 (cross) ↑	0.33	0.56	**0.75**	0.31	0.67	**0.74**	0.14	0.46	**0.57**

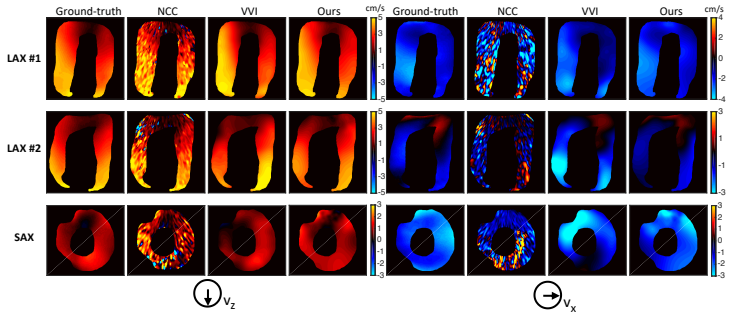

Fig. 4. Velocity fields in the X and Z dimensions of the STRAUS dataset in LAX #1, LAX #2, and SAX views in the phased array imaging. The X and Z velocity components are transformed from the in-range and cross-range estimates.

3.2 Results

Fig. 3 shows the in-range and cross-range velocity fields of the spinning disk at 20 cm/s in the linear array imaging. Our method achieves the most similar estimates to the ground truths. In comparison, VVI introduces more variance to the estimates, whereas NCC makes wrong axial estimates in the region with high axial velocities and underestimates the peak lateral velocities.

Table 2 summarizes the quantitative results on STRAUS in phased array imaging. Our method improves nRMSE by 8.84% in LAX #1, 19.21% in LAX #2, and 10.94% in SAX over VVI. Fig. 4 shows the velocity fields in LAX #1, LAX #2, and SAX obtained by the tested methods. VVI and our method

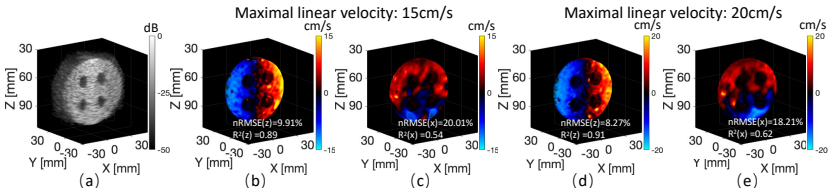

Fig. 5. Volumetric rendering of the 3D velocity fields in the central X-Z cross-section: (a) is B-mode image. (b) and (c) are velocities in the Z and X dimensions at 15 cm/s; (d) and (e) show the results at 20 cm/s.

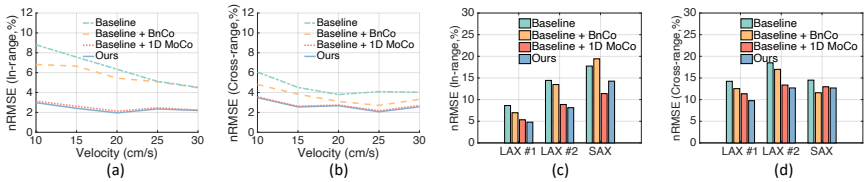

Fig. 6. Ablation study in phased array imaging. (a) and (b) are the nRMSE of the Z-direction and X-direction velocity fields on the spinning disk. (c) and (d) are the nRMSE of Z-direction and X-direction velocity fields on STRAUS.

provide similar results in LAX #1 and Z-direction velocities of SAX. However, our method performs better in LAX #2 and X-direction velocities of SAX. In comparison, NCC introduces artifacts in the Z-direction.

Fig. 5 shows the Z and X-velocity components derived from the in-range and cross-range velocity fields in the matrix array imaging. The nRMSE and R^2 of the Z velocity components are much better than those of the X components due to the smaller aperture size of the matrix array (9.3 mm), resulting in a much lower sensitivity of volumetric imaging to motions in the X-direction.

3.3 Ablation Study

The ablation study was conducted in phased array imaging. Four configurations were tested: baseline, baseline + BnCo, baseline + MoCo, and baseline + BnCo + MoCo. Fig. 6(a)-(b) shows the nRMSE results on the spinning disk, showing that BnCo, 1D MoCo, and their combination can improve velocity field estimation. Fig. 6(c)-(d) presents the nRMSE results on STRAUS. 1D in-range MoCo and BnCo both contribute positively to the in-range and cross-range velocity estimation in LAX #1 and LAX #2. However, BnCo negatively impacts the in-range estimation in SAX. This may be because BnCo also amplifies noise during sound field equalization, thus deteriorating the low-velocity estimations in SAX.

4 Conclusion

This paper proposes a uniform multi-mode (Doppler and pair-wise optical flow) fused framework for tissue velocity field estimation in ultrasound. This model is also adapted to multiple ultrasound imaging schemes. The *in-silico* experimental results demonstrated the performance of the proposed method. The ablation study further demonstrated the effectiveness of the proposed BnCo and 1D in-range MoCo. Improving the accuracy of the cross-range velocity fields in matrix array imaging and *in-vivo* validations are the future directions of this work.

Acknowledgments. This work was supported by the Natural Science Foundation of Xiamen, China (No. 3502Z202473004), the Wang Deyao Outstanding Graduate Scholarship Program of Xiamen University, the Fujian Provincial Natural Science Foundation of China (No. 2024J01003), the National Natural Science Foundation of China (No. 62471416), and the Fundamental Research Funds for the Central Universities (No. 20720240075).

Disclosure of Interests. The authors have no competing interests to declare that are relevant to the content of this article.

References

1. Alessandrini, M., De Craene, M., Bernard, O., Giffard-Roisin, S., Allain, P., Waechter-Stehle, I., Weese, J., Saloux, E., Delingette, H., Sermesant, M., D'hooge, J.: A pipeline for the generation of realistic 3d synthetic echocardiographic sequences: Methodology and open-access database. IEEE Transactions on Medical Imaging **34**(7), 1436–1451 (2015)
2. Ashikuzzaman, M., Héroux, A., Tang, A., Cloutier, G., Rivaz, H.: Displacement tracking techniques in ultrasound elastography: From cross correlation to deep learning. IEEE Transactions on Ultrasonics, Ferroelectrics, and Frequency Control **71**(7), 842–871 (2024)
3. Chen, Y., D'hooge, J., Luo, J.: Doppler-based motion compensation strategies for 3-d diverging wave compounding and multiplane-transmit beamforming: A simulation study. IEEE Transactions on Ultrasonics, Ferroelectrics, and Frequency Control **65**(9), 1631–1642 (2018)
4. Chen, Y., Zhuang, Z., Luo, J., Luo, X.: Doppler and pair-wise optical flow constrained 3d motion compensation for 3d ultrasound imaging. IEEE Transactions on Image Processing **32**, 4501–4516 (2023)
5. Delaunay, R., Hu, Y., Vercauteren, T.: An unsupervised approach to ultrasound elastography with end-to-end strain regularisation. In: Medical Image Computing and Computer Assisted Intervention – MICCAI 2020. pp. 573–582. Springer International Publishing, Cham (2020)
6. Delaunay, R., Hu, Y., Vercauteren, T.: An unsupervised learning approach to ultrasound strain elastography with spatio-temporal consistency. Physics in Medicine & Biology **66**(17), 175031 (sep 2021)

7. Dosovitskiy, A., Fischer, P., Ilg, E., Häusser, P., Hazirbas, C., Golkov, V., Smagt, P.v.d., Cremers, D., Brox, T.: Flownet: Learning optical flow with convolutional networks. In: 2015 IEEE International Conference on Computer Vision (ICCV). pp. 2758–2766 (2015)
8. Evain, E., Faraz, K., Grenier, T., Garcia, D., De Craene, M., Bernard, O.: A pilot study on convolutional neural networks for motion estimation from ultrasound images. IEEE Transactions on Ultrasonics, Ferroelectrics, and Frequency Control **67**(12), 2565–2573 (2020)
9. Hui, T.W., Tang, X., Loy, C.C.: Liteflownet: A lightweight convolutional neural network for optical flow estimation. In: 2018 IEEE/CVF Conference on Computer Vision and Pattern Recognition. pp. 8981–8989 (2018)
10. Ilg, E., Mayer, N., Saikia, T., Keuper, M., Dosovitskiy, A., Brox, T.: Flownet 2.0: Evolution of optical flow estimation with deep networks. In: 2017 IEEE Conference on Computer Vision and Pattern Recognition (CVPR). pp. 1647–1655 (2017)
11. Jensen, J., Svendsen, N.: Calculation of pressure fields from arbitrarily shaped, apodized, and excited ultrasound transducers. IEEE Transactions on Ultrasonics, Ferroelectrics, and Frequency Control **39**(2), 262–267 (1992)
12. Kibria, M.G., Hasan, M.K.: A class of kernel based real-time elastography algorithms. Ultrasonics **61**, 88–102 (2015)
13. Li, H., Porée, J., Chayer, B., Cardinal, M.H.R., Cloutier, G.: Parameterized strain estimation for vascular ultrasound elastography with sparse representation. IEEE Transactions on Medical Imaging **39**(12), 3788–3800 (2020)
14. Luo, J., Konofagou, E.E.: A fast normalized cross-correlation calculation method for motion estimation. IEEE Transactions on Ultrasonics, Ferroelectrics, and Frequency Control **57**(6), 1347–1357 (2010)
15. Porras, A.R., Alessandrini, M., De Craene, M., Duchateau, N., Sitges, M., Bijnens, B.H., Delingette, H., Sermesant, M., D'hooge, J., Frangi, A.F., Piella, G.: Improved myocardial motion estimation combining tissue doppler and b-mode echocardiographic images. IEEE Transactions on Medical Imaging **33**(11), 2098–2106 (2014)
16. Porée, J., Baudet, M., Tournoux, F., Cloutier, G., Garcia, D.: A dual tissue-doppler optical-flow method for speckle tracking echocardiography at high frame rate. IEEE Transactions on Medical Imaging **37**(9), 2022–2032 (2018)
17. Porée, J., Posada, D., Hodzic, A., Tournoux, F., Cloutier, G., Garcia, D.: High-frame-rate echocardiography using coherent compounding with doppler-based motion-compensation. IEEE Transactions on Medical Imaging **35**(7), 1647–1657 (2016)
18. Ranjan, A., Black, M.J.: Optical flow estimation using a spatial pyramid network. In: 2017 IEEE Conference on Computer Vision and Pattern Recognition (CVPR). pp. 2720–2729 (2017)
19. Sigrist, R.M., Liau, J., Kaffas, A.E., Chammas, M.C., Willmann, J.K.: Ultrasound elastography: Review of techniques and clinical applications. Theranostics **7**, 1303–1329 (2017)
20. Suhling, M., Arigovindan, M., Jansen, C., Hunziker, P., Unser, M.: Myocardial motion analysis from b-mode echocardiograms. IEEE Transactions on Image Processing **14**(4), 525–536 (2005)
21. Sun, D., Yang, X., Liu, M.Y., Kautz, J.: Pwc-net: Cnns for optical flow using pyramid, warping, and cost volume. In: 2018 IEEE/CVF Conference on Computer Vision and Pattern Recognition. pp. 8934–8943 (2018)
22. Wei, X., Wang, Y., Ge, L., Peng, B., He, Q., Wang, R., Huang, L., Xu, Y., Luo, J.: Unsupervised convolutional neural network for motion estimation in ultrasound

elastography. IEEE Transactions on Ultrasonics, Ferroelectrics, and Frequency Control **69**(7), 2236–2247 (2022)
23. Wu, S., Gao, Z., Liu, Z., Luo, J., Zhang, H., Li, S.: Direct reconstruction of ultrasound elastography using an end-to-end deep neural network. In: Medical Image Computing and Computer Assisted Intervention – MICCAI 2018. pp. 374–382. Springer International Publishing, Cham (2018)
24. Yang, X., Yan, J., Chen, Z., Ding, H., Liu, H.: A proportional pattern recognition control scheme for wearable a-mode ultrasound sensing. IEEE Transactions on Industrial Electronics **67**(1), 800–808 (2020)